Neuronal cell adhesion molecule (NRCAM) variant defined by microexon skipping is an essential, antigenically distinct, and targetable proteoform in high-grade glioma

Priyanka Sehgal[1], Ammar S. Naqvi[2], Makenna Higgins[1], Jiageng Liu[3] , Kyra Harvey[4], Julien Jarroux[5], Taewoo Kim[5], Berk Mankaliye[5], Pamela Mishra[1,6], Grace Watterson[7], Justyn Fine[8], Jacinta Davis[1], Katharina E. Hayer[1,6], Annette Castro[1], Adanna Mogbo[9], Charles Drummer 4th[1], Daniel Martinez[10], Mateusz P. Koptyra[2], Zhiwei Ang[1], Kai Wang[11,12], Alvin Farrel[6], Mathieu Quesnel-Vallieres[13%], Yoseph Barash[13], Jamie B. Spangler[8,14], Jo Lynne Rokita[2#], Adam C. Resnick[2], Hagen U. Tilgner[5,15], Thomas DeRaedt[4], Daniel J Powell Jr[11], and Andrei Thomas-Tikhonenko[1,7,11*]

[1]Division of Cancer Pathobiology, Children's Hospital of Philadelphia, Philadelphia, PA
[2]Center for Data-Driven Discovery in Biomedicine, Children's Hospital of Philadelphia, Philadelphia, PA
[3]Department of Bioengineering, University of Pennsylvania, Philadelphia, PA
[4]Division of Oncology, Children's Hospital of Philadelphia, Philadelphia, PA
[5]Center for Neurogenetics, Brain and Mind Research Institute, Weill Cornell Medicine, New York, NY
[6]Department of Biomedical & Health Informatics, Children's Hospital of Philadelphia, Philadelphia, PA
[7]Cell and Molecular Biology Graduate Group, University of Pennsylvania, Philadelphia, PA
[8]Program in Molecular Biophysics, Johns Hopkins University, Baltimore, MD
[9]Vagelos Life Sciences Management Program, University of Pennsylvania, Philadelphia, PA
[10] Pathology Core, Children's Hospital of Philadelphia, Philadelphia, PA
[11]Department of Pathology & Laboratory Medicine, University of Pennsylvania, Philadelphia, PA
[12]Center for Cellular and Molecular Therapeutics, Children's Hospital of Philadelphia, Philadelphia, PA
[13]Department of Genetics, University of Pennsylvania, Philadelphia, PA
[14]Department of Chemical & Biomolecular Engineering, Johns Hopkins University, Baltimore, MD
[15]Helen and Robert Appel Alzheimer's Disease Research Institute, Weill Cornell Medicine, New York, NY

[#] present address: Center for Cancer and Immunology Research, Children's National Hospital, Washington, DC
[%] present address: Département d'immunologie et de biologie cellulaire, Université de Sherbrooke, Sherbrooke, QC
**corresponding author: andreit@pennmedicine.upenn.edu*

Conflict of interest statement: the authors declare no potential conflicts of interest

Abstract

To overcome the paucity of known tumor-specific surface antigens in pediatric high-grade glioma (pHGG), we contrasted splicing patterns in pHGGs and normal brain samples. Among alternative splicing events affecting extracellular protein domains, the most pervasive alteration was the skipping of ≤30 nucleotide-long microexons. Several of these skipped microexons mapped to L1-IgCAM family members, such as *NRCAM*. Bulk and single-nuclei short- and long-read RNA-seq revealed uniform skipping of *NRCAM* microexons 5 and 19 in virtually every pHGG sample. Importantly, the Δex5Δex19 (but not the full-length) NRCAM proteoform was essential for pHGG cell migration and invasion in vitro and tumor growth in vivo. We developed a monoclonal antibody selective for Δex5Δex19 NRCAM and demonstrated that "painting" of pHGG cells with this antibody enables killing by T cells armed with an FcRI-based universal immune receptor. Thus, pHGG-specific NRCAM and possibly other L1-IgCAM proteoforms are promising and highly selective targets for adoptive immunotherapies.

Statement of significance

Existing targets for chimeric antigen receptors (CAR)-armed T cells are often shared by CNS tumors and normal tissues, creating the potential for on-target/off-tumor toxicities. Here we demonstrate that in CNS tumors of glial origin, cell adhesion molecules have alternatively spliced proteoforms, which could be targeted by highly selective therapeutic antibodies.

Introduction

Pediatric high-grade gliomas (pHGG) are some of the most recalcitrant, chemoresistant, and often surgically unresectable childhood cancers. For example, children affected by diffuse midline gliomas (DMG) nearly universally succumb to the disease within 8-10 months of diagnosis (1). Its adult counterpart, glioblastoma multiforme (GBM), is equally lethal (2). Currently, there are no effective standard of care therapies for these patients, despite decades of molecularly agnostic clinical trials, underscoring the importance of developing novel immunotherapies. Several targets for CAR T cells in GBM have been developed, most notably EGFRvIII (3,4), HER2 (5), IL13Rα2 (6), and Eph2A (7), but so far the corresponding immunotherapeutics enjoyed limited success in the clinic, owing in part to the frequent emergence of antigen escape variants [reviewed in (8-11)].

Although GBMs and pHGGs are thought to arise in the same lineage, the latter express somewhat different repertoires of surface antigens. Validated pHGG targets include GD2 and B7-H3 [reviewed in (12,13)]. GD2 in particular is highly expressed by H3K27M-mutated DMG cells (14), and the first 4 DMG patients were recently treated with anti-GD2 CAR, with some clinical and radiographic improvement (15). Similarly, both anaplastic astrocytomas and DMG express B7-H3 (a.k.a. CD276), and an anti-B7-H3 CAR has shown activity in preclinical models of pediatric tumors (16). However, targeting GD2 is associated with well-documented (although not universally observed) on-target, off-tumor toxicities (17,18), and side effects of another anti-B7-H3 CAR have been only assessed in the mouse (19) and in the first three evaluable human patients with DIPG (20).

Even if GD2- and/or B7-H3-directed immunotherapies become standards of care, the clinical use of CAR T cells in patients with hematologic malignancies suggests that there is no such thing as the "perfect" target, and there cannot be too many alternatives (21,22), the more cancer-specific the better (23). Here we describe our effort to systemically identify new targets using as a model pHGG, where mutation burden is typically low, and aberrant mRNA splicing is a key post-transcriptional mechanism of proteome diversification (24). This effort has led to identification of the four members of the L1-immunoglobulin (Ig) sub-family of cell adhesion molecules (CAMs), in particular NRCAM splice variant, as promising targets for adoptive T cell therapy.

Results

Identification of microexon-derived surface proteoforms in pHGG. Our initial analysis of 325 pHGG tumors from the Open Pediatric Brain Tumor Atlas (25) revealed that not only is aberrant splicing prevalent in pHGG, but these tumors had some of the most heterogeneous splicing programs (24). Thus, the rMATS splicing algorithm (26) was used to compare 184 pHGG patient samples to each of the 7 healthy controls comprised of an adult brain homogenate, an adult brain stem, an adult cerebellum, an adult occipital cortex, two fetal brains, and one pediatric normal cortex. pHGG-specific splice junction candidates were filtered for single-exon (SE) events, whose junctions were mapped to predicted protein structures using UniProt annotations and filtered for SE events corresponding to extracellular protein domains (Figure 1A).

These events were filtered for 40% prevalence and further binned according to exon lengths. The only events with mean differences in percent-spliced-in (ΔPSI) absolute values greater than 0.50 were skipping of very short exons: ≤30- and 31-50-nucleotide long (Figure 1B). These are known as microexons (27), and their dysregulation has been previously implicated in several CNS diseases (28), including autism spectrum disorder (29). Inclusion of microexons requires dedicated RNA binding proteins such as RBFOX (30,31) and SRRM4 (29,32-34), whose activity is counteracted by PTBP1, a promoter of microexon skipping (35-37). Of note, expression levels of *RBFOX1* and *SRRM4* mRNA were lower, and that of *PTBP1* were higher in pHGG compared to normal brain tissues (Figure 1C), which could explain the observed bias toward microexon skipping.

Thus, we re-analyzed the entire rMATS output focusing on microexons corresponding to cell surface proteins and with |ΔPSI|≥0.5. We found that mRNAs encoding the 4 members of the L1-immunoglobulin superfamily of cell adhesion molecules (IgCAM), *L1CAM* itself, *NFASC*, *CHL1*, and *NRCAM*, were among the most profoundly and consistently mis-spliced transcripts (Figure 1D,E). In fact, neuronal cell adhesion molecule (*NRCAM*) mRNA had two microexon-related events: skipping of the 18-nt microexon 5 and the 30-nt microexon 19 [MANE nomenclature (38); exons 9 and 23 in GTEx v8 (39)] (Figure 1E). We also observed skipping of microexon 7 in *L1CAM* and microexon 24 in *NFASC*. One exception to the trend toward exon skipping was increased inclusion of exon 8 in *CHL1*, but that exon was slightly longer, 48 nucleotides, which is borderline for the purpose of microexon definition (40).

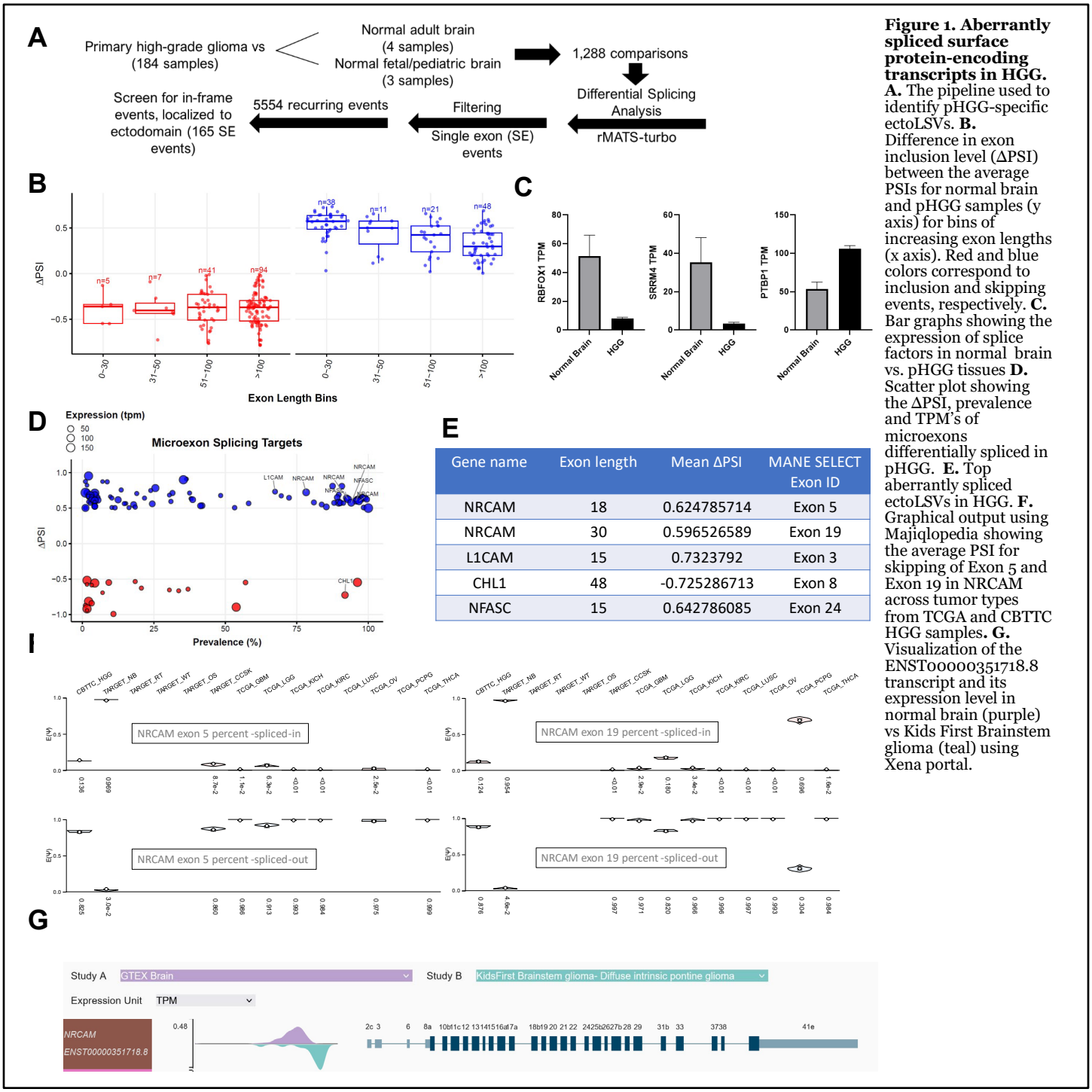

Figure 1. Aberrantly spliced surface protein-encoding transcripts in HGG. A. The pipeline used to identify pHGG-specific ectoLSVs. **B.** Difference in exon inclusion level (ΔPSI) between the average PSIs for normal brain and pHGG samples (y axis) for bins of increasing exon lengths (x axis). Red and blue colors correspond to inclusion and skipping events, respectively. **C.** Bar graphs showing the expression of splice factors in normal brain vs. pHGG tissues **D.** Scatter plot showing the ΔPSI, prevalence and TPM's of microexons differentially spliced in pHGG. **E.** Top aberrantly spliced ectoLSVs in HGG. **F.** Graphical output using Majiqlopedia showing the average PSI for skipping of Exon 5 and Exon 19 in NRCAM across tumor types from TCGA and CBTTC HGG samples**. G.** Visualization of the ENST00000351718.8 transcript and its expression level in normal brain (purple) vs Kids First Brainstem glioma (teal) using Xena portal.

Focusing on *NRCAM* as the most profoundly affected transcript, we asked whether its microexons are skipped in other human tumors. We queried MAJIQlopedia, our recently developed compendium of splicing variations across 86 human tissues and 41 cancer datasets (41). We found that skipping of *NRCAM* exons 5 and 19 was prevalent in all tumor types with detectable *NRCAM* splice junctions (Supplemental Figure S1C). They included pHGG, adult low-grade gliomas and GBMs, pheochromocytomas and paragangliomas, and also cancers of non-neural origins, such lung adenocarcinomas (Figure 1F). The sole exception was pediatric neuroblastoma, where *NRCAM* exons 5 and 19 were uniformly included. Of note, these splicing quantifications were based on MAJIQ (42), an algorithm orthogonal to rMATS, increasing our confidence in *NRCAM*-centric events. Further evidence for preferential *NRCAM* exon 5 and 19 skipping in pHGG was found in the output of Toil, yet another orthogonal approach to transcript reconstitution from short-read RNA-seq data (43). Using Xena portal (44), we observed that transcript ENST00000351718.8 lacking exons 5 and 19 was overexpressed in brainstem gliomas compared to normal brain tissues (Figure 1G). ENST00000351718.8 was also upregulated in GBMs, consistent with the MAJIQlopedia output (Supplemental Figure S1A).

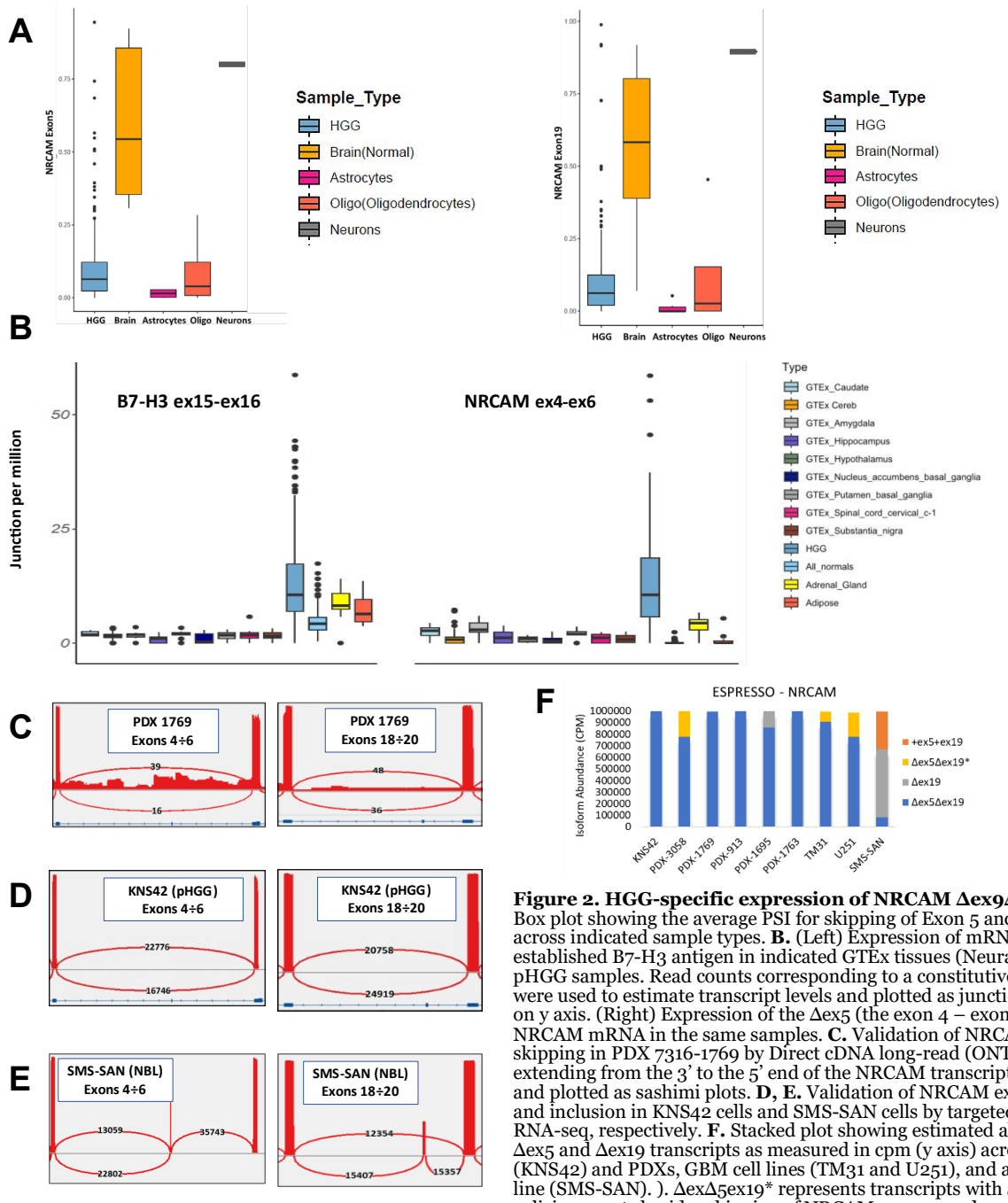

Figure 2. HGG-specific expression of NRCAM Δex9Δex23 isoform. A. Box plot showing the average PSI for skipping of Exon 5 and Exon 19 in NRCAM across indicated sample types. **B.** (Left) Expression of mRNA encoding the established B7-H3 antigen in indicated GTEx tissues (Neural- and non-neural) and pHGG samples. Read counts corresponding to a constitutive exon-exon junction were used to estimate transcript levels and plotted as junction per million counts on y axis. (Right) Expression of the Δex5 (the exon 4 – exon 6 junction) isoform of NRCAM mRNA in the same samples. **C.** Validation of NRCAM exon 5 and 19 skipping in PDX 7316-1769 by Direct cDNA long-read (ONT) RNA-seq. Reads extending from the 3' to the 5' end of the NRCAM transcript were visualized in IGV and plotted as sashimi plots. **D, E.** Validation of NRCAM exon 5 and 19 skipping and inclusion in KNS42 cells and SMS-SAN cells by targeted long-read (ONT) RNA-seq, respectively. **F.** Stacked plot showing estimated abundances of NRCAM Δex5 and Δex19 transcripts as measured in cpm (y axis) across pHGG cell lines (KNS42) and PDXs, GBM cell lines (TM31 and U251), and a neuroblastoma cell line (SMS-SAN).). ΔexΔ5ex19* represents transcripts with additional alternative splicing events besides skipping of NRCAM exons 5 and exon19.

HGG-specific expression of NRCAM Δex5Δex19 isoform. To determine whether microexon skipping reflects, at least to some extent, HGG lineage, we included in the analysis the RNA-seq dataset corresponding to 20 human primary astrocyte samples, 1 neuron sample, and 4 oligodendrocytes (45). We observed that skipping of HGG-specific microexons occurred primarily in astrocytes and oligodendrocytes, but not neurons, consistent with the pHGG eponymous cell of origin.

PSI values, while reflective of the underlying molecular mechanism, do not yield information about expression levels of a given isoform, which are much more relevant from the immunotherapy standpoint. Thus, we complemented our splicing analysis with the parsing of splice junction counts, which is one of the key outputs of the STAR aligner (46). Specifically, we quantified expression of the non-canonical exon 4-exon 6 junctions in pHGG samples and across the GTEx dataset comprised of both neuronal and non-neuronal normal tissues. *B7-H3/CD276* canonical exon 15-exon 16 junction was used for comparison. We observed that *NRCAM* Δex5Δex19 and *B7-H3* transcripts were expressed at comparable levels in pHGG and brain sub-regions, while *NRCAM* Δex5Δex19 had the advantage of being expressed at lower levels in non-neuronal normal organs, such as the adrenal gland and the adipose tissue (Figure 2B). Similar results were obtained using as a readout *NRCAM*

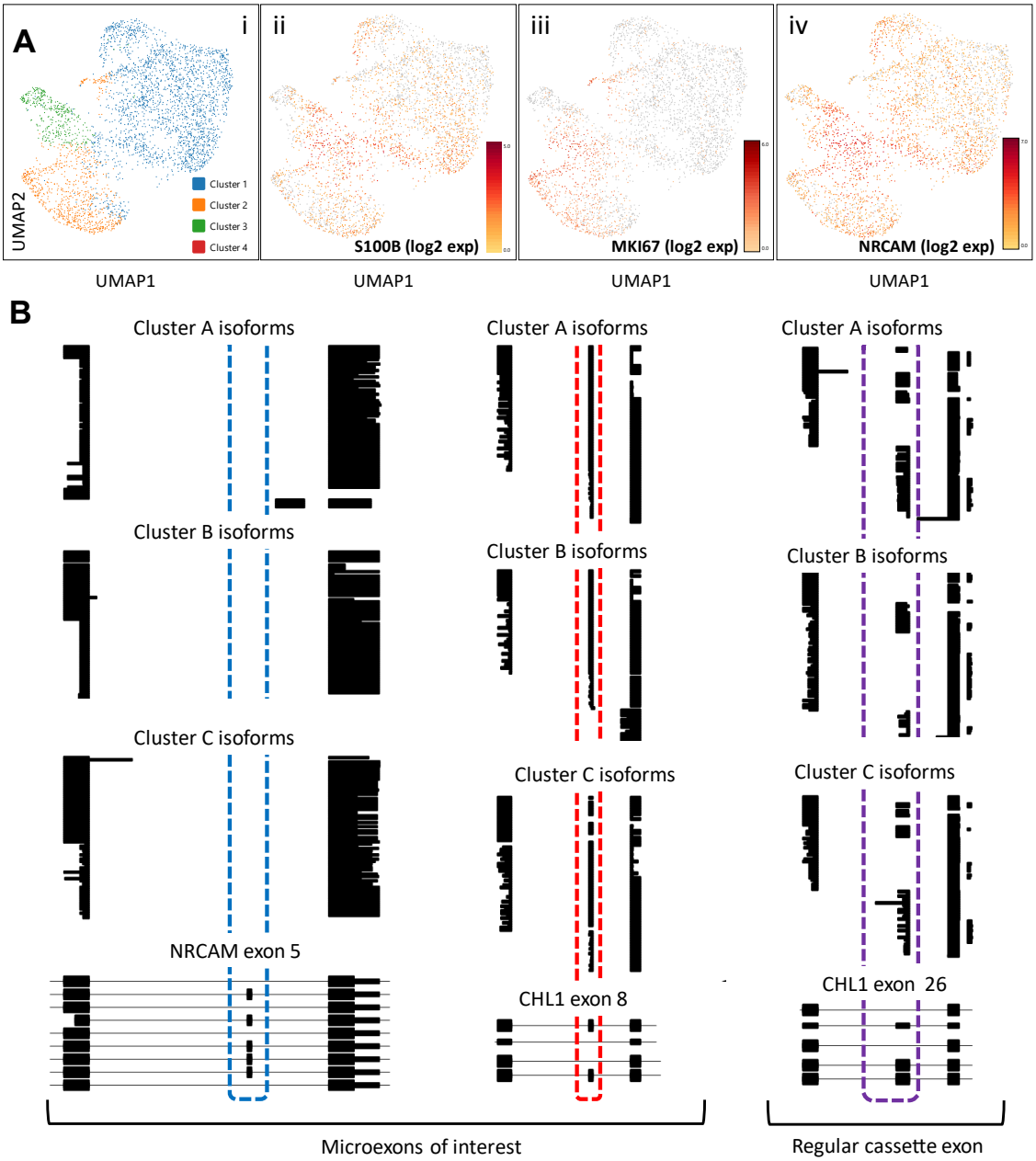

Figure 3. Single-nuclei analysis of PDX 7316-3058. A. Short-read RNA-seq analysis (10x genomic platform) of >3,700 nuclei sequenced using 10x Genomics platform. Uniform Manifold Approximation and Projection (UMAP) plots were generated using Cell Ranger analysis and colored by cell-type annotation (i). Additional UMAP plots of the same cells were colored by expression of individual genes using Loupe Browser (i-iv). **B.** Long-read RNA-seq analysis of full-length transcripts. ScisorWiz plots show reads spanning exons of interest in NRCAM and CHL1 genes (dotted rectangles) and grouped by clusters. Each horizontal line indicates one transcript; thick blocks denote exons, and thin lines denote introns (not drawn to scale to aid visualization). Bottom panels show annotated GENCODE transcripts.

exon 18-exon 20 junction (Supplemental Figure S1B, top left.) The other three members of the *L1CAM* family showed the same pattern of elective exon usage, except that their expression levels in pHGG were markedly lower (Supplemental Figure S1B, top right and bottom).

To determine whether skipping of *NRCAM* microexons 5 and 19 occurs concurrently and in the context of functional, cap-to-poly(A) transcripts, we performed direct cDNA long-read sequencing using Oxford Nanopore platform Promethion P2 for two DMG PDX samples, 7316-1763 and 7316-1769. To ensure accurate detection of small exons, STAR-aligned reads were realigned using MisER (47). We observed skipping of both *NRCAM* exon 5 and exon 19 in PDX 7316-1769 (Figure 2C), however due to low read depth we could not detect any transcripts for *NRCAM* in PDX 7316-1763. To circumvent the read depth issues, we performed targeted long-read re-sequencing on several PDX samples, KNS42 pHGG cell line, TM31 and U251 GBM cell lines, and SMS-SAN neuroblastoma cell line. Direct examination of sequencing reads in the Integrative Genomics Viewer [IGV; (48)] revealed that all oligo(dT)-primed *NRCAM* transcripts extending to the 5' end lacked exons 5 and 19 in KNS42 cells, but included them at ~50% frequency in SMS-SAN NBL (Figure 2D,E). Using the ESPRESSO computational tool (49), we quantified the expression of various *NRCAM* transcripts in all sequenced samples. We observed that all pHGG and GBM cell lines and PDXs predominantly express the *NRCAM* variant lacking both exon 5 and exon 19 (Figure 2F, blue, grey, and yellow bars), while in SMS-SAN cells inclusion of exon 19 was common (orange bar) and skipping of both exon 5 and exon 19 was rather rare.

Assessment of tumor heterogeneity by single-cell long-read-seq. Bulk long-read RNA sequencing is commonly used to identify full-length transcripts, but initially it did not have single-cell resolution capabilities (50,51). Subsequent single-cell long-read approaches were developed for fewer than 100 cells (52,53), making the assessment of tumor heterogeneity difficult. To overcome this limitation, we recently developed techniques for long-read sequencing of thousands of single cells from both fresh [ScISOr-Seq; (54)] and frozen [SnISOr-Seq; (55)] tissues. The most recent iteration of this approach [(SnISOr-Seq/ScISOr-ATAC; (55,56)] allows for the accurate cataloging of full-length transcripts devoid of intronic sequences. We applied this approach to DMG PDX 7316-3058. According to the short-read dataset (the 10x Genomics part of the workflow), this sample can be broken down into 4 clusters based on K-means (Figure 3A, panel i). Parsing of individual gene expression data revealed that all cells are predominantly grey matter protoplasmic astrocytes, as evidenced by S100B expression (panel ii). However, proliferating cells are largely confined to Cluster 2, as evidenced by expression of the *MKI67* gene (panel iii). Nevertheless, virtually all neoplastic cells, regardless of cluster attribution, robustly expressed *NRCAM* mRNA (panel iv).

Then, using the long-read dataset (the long-read-seq part of the workflow), we asked how microexons of interest are represented in the 3 major clusters (A, B, and C in Figure 3B). This was achieved by retaining barcoded reads only and aligning them over GRCh39 genome by minimap2 with gencode v44 gtf as described earlier (57). When we examined ScisorWiz (55) plots. we observed that all recovered reads for *NRCAM* exons 4 and 6 skipped microexon 5 (blue dotted rectangle) and all recovered reads for *CHL1* exons 7 and 9 included microexon 8 (red rectangle), with no evidence of intra- or inter-cluster heterogeneity. This was in sharp contrast with the *CHL1* "non-micro" cassette exon 26, whose inclusion and skipping varied considerably both within and among the 3 clusters (purple rectangle). Collectively, these results suggested that in pHGG *L1-CAM* microexons are processed in a uniform, rather than a stochastic manner, making the corresponding proteoforms much more compelling immunotherapy targets.

The role of Δex5Δex19 NRCAM in pHGG pathogenesis. To determine whether this aberrantly spliced NRCAM isoform is expressed on the plasma membrane, we adapted a whole-cell biotinylation assay for the KNS42 pHGG line, as described in Materials and Methods. Briefly, live cells were incubated with biotin to label Lys residues of surface proteins, which upon lysis were isolated using neutravidin beads and analyzed by immunoblotting. In these subcellular localization experiments, EGFR served as a reference cell surface marker and tubulin and actin as cytosolic markers. As additional controls, we generated via CRISPR/Cas9 editing *NRCAM* knockout (KO) KNS42 cells and validated the loss of NRCAM expression using a commercially available anti-NRCAM antibody (Figure 4A). We reliably observed the Δex5Δ19 NRCAM isoform in both total cell lysate and the cell surface but not cytosolic ("flow-through") fractions and largely absent from all NRCAM KO cells fraction (Figure 4B). This result is in line with multiple reports showing that microexon-encoded amino acids are typically located on outer surfaces and regulate protein-protein interactions, rather than surface localization (40).

To determine the role of the skipped isoform of NRCAM in pHGG, we reconstituted NRCAM KO cells with the full-length (exon 5-/exon 19-including) and the Δex5Δ19 NRCAM isoform and confirmed their expression by immunoblotting (Figure 4C). Compared to vector control cells, neither of them showed any effect on cell proliferation in 2-D cultures (Figure 4D). However, the Δex5Δex19 - but not the full-length NRCAM isoform - enhanced migration and invasion by KNS42 cells, as evidenced by the Transwell assays performed with and without Matrigel (Figure 4E, F), as described by us previously (58).

Finally, we modified these cells to express firefly luciferase and implanted them orthotopically into the cortexes of NSG mice, as described previously (59). We observed more consistent tumor take and substantially more robust tumor growth when the Δex5Δex19 NRCAM isoform was expressed, whereas both *NRCAM*-null and *NRCAM*-full length KNS42 cells took and grew rather poorly (Figure 4G,H). In fact, mice bearing these tumors were still alive on Day 120, while their Δex5Δex19 counterparts were all dead by day 30 (Figure 4I). The apparent essentiality of Δex5Δex19 for tumor growth and its uniform expression on the cell surface made it an attractive target for pHGG immunotherapy.

pHGG-selective anti-NRCAM antibodies and their therapeutic utility. Given the minimal difference in the amino acid sequences between the full-length and the Δex5Δex19 NRCAM proteoforms, we used AlphaFold 3 (60) to predict 3D structural models for the corresponding Uniprot-annotated ectodomains. It predicted a "horseshoe" conformation with a hinge between Ig-like 2 and Ig-like 3 domains in both isoforms, similar to crystal structures of another L1 family-member, L1CAM [(61); discussed in (62)]. AlphaFold 3 also predicts that the proline-rich microexon 19-encoded amino acid sequence creates a sharp bend between Ig-like 6 domain and the first fibronectin type-III domain (Figure 5A, left). This bend is absent from the

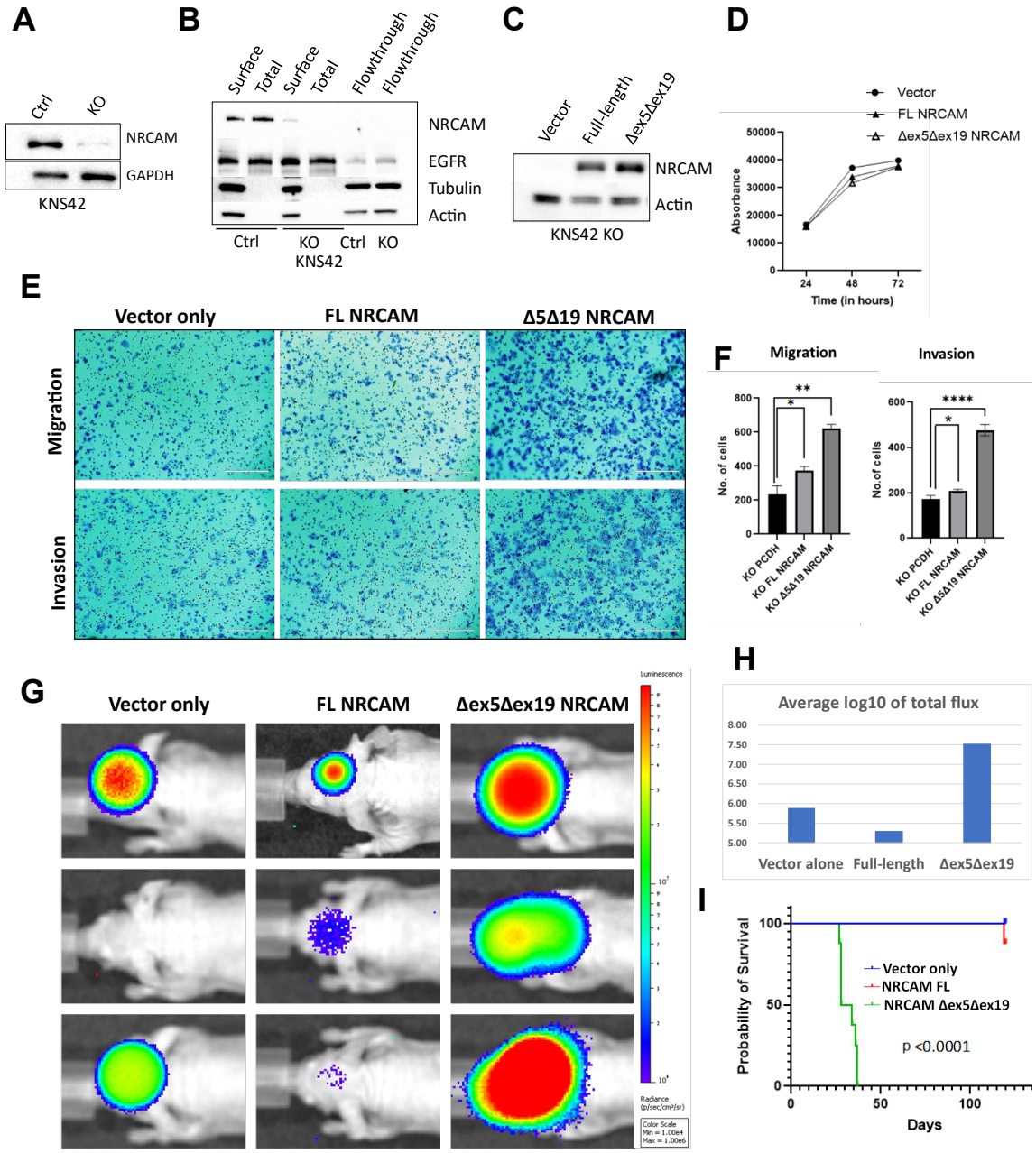

Figure 4. Aberrantly spliced NRCAM proteoforms in pHGG. A. Immunoblotting showing NRCAM levels in KNS42 HGG cells transfected with NRCAM-targeting gRNAs. GAPDH served as loading control. **B.** Immuno-blotting showing levels of Full-length and Δex5Δex19 NRCAM isoforms in cell-surface, flow-through fractions, and total cell lysates of KNS42 wild-type and NRCAM KO cells. EGFR, Tubulin and Actin were used as controls. **C.** Immuno-blotting showing NRCAM levels in KNS42 NRCAM KO cells reconstituted with the full length (FL) or the Δex5Δex19 NRCAM isoforms. **D.** 72 h proliferation rates of NRCAM KO cells expressing the canonical or the Δex5Δex19 NRCAM isoforms. **E.** Migration (top) and invasion (bottom) potential of NRCAM KO cells re-expressing canonical and Δex5Δ19 isoforms of NRCAM. The Transwell assays were performed with or without Matrigel, respectively. **F.** Quantitation of migrated and invaded cells from G. Each bar represents mean ± SEM. Significance (asterisks) was determined using unpaired Student's t-test. **G.** Optical imaging of the same cells additionally engineered to expressed firefly luciferase after orthotopic injection in the cortex of NSG mice (Day 28). **H.** Raw photon counts corresponding to tumors in panel G. **I.** Kaplan-Meier survival curve of mice depicted in panel G with p value determined by Log-rank (Mantel-Cox) test.

NRCAMΔex5Δex19 proteoform model, creating a more open conformation that could be available for selective targeting (Figure 5A, right).

To generate NRCAM Δex5Δex19-selective monoclonal antibodies, we expressed this isoform in murine NIH3T3 cells and immunized syngeneic C57BL/J mice with whole cells using the Fred Hutchinson Cancer Center Antibody Technology Core Facility (Figure 5B), as described by others previously (63). Supernatants from the resultant hybridomas were used to stain CHO cells expressing either the full-length or the Δex5Δex19 NRCAM proteoform. As expected, the majority of mAbs (exemplified by 2D10 in Figure 5C) stained both the full-length and the Δex5Δex19 NRCAM isoforms equally well (grey arrows). However, mAb 3F8 showed selectivity for NRCAM Δex5Δex19, as judged by ~10-fold difference in mean fluorescent intensities (Figure 5D, grey and gold arrows). Importantly, this binder recognized the endogenously expressed Δex5Δex19 NRCAM in pHGG samples, such as the KNS42 cell line (Figure 5E, purple peak with orange arrow), even though non-specific, background staining was also observed in *NRCAM* KO cells (green peak).

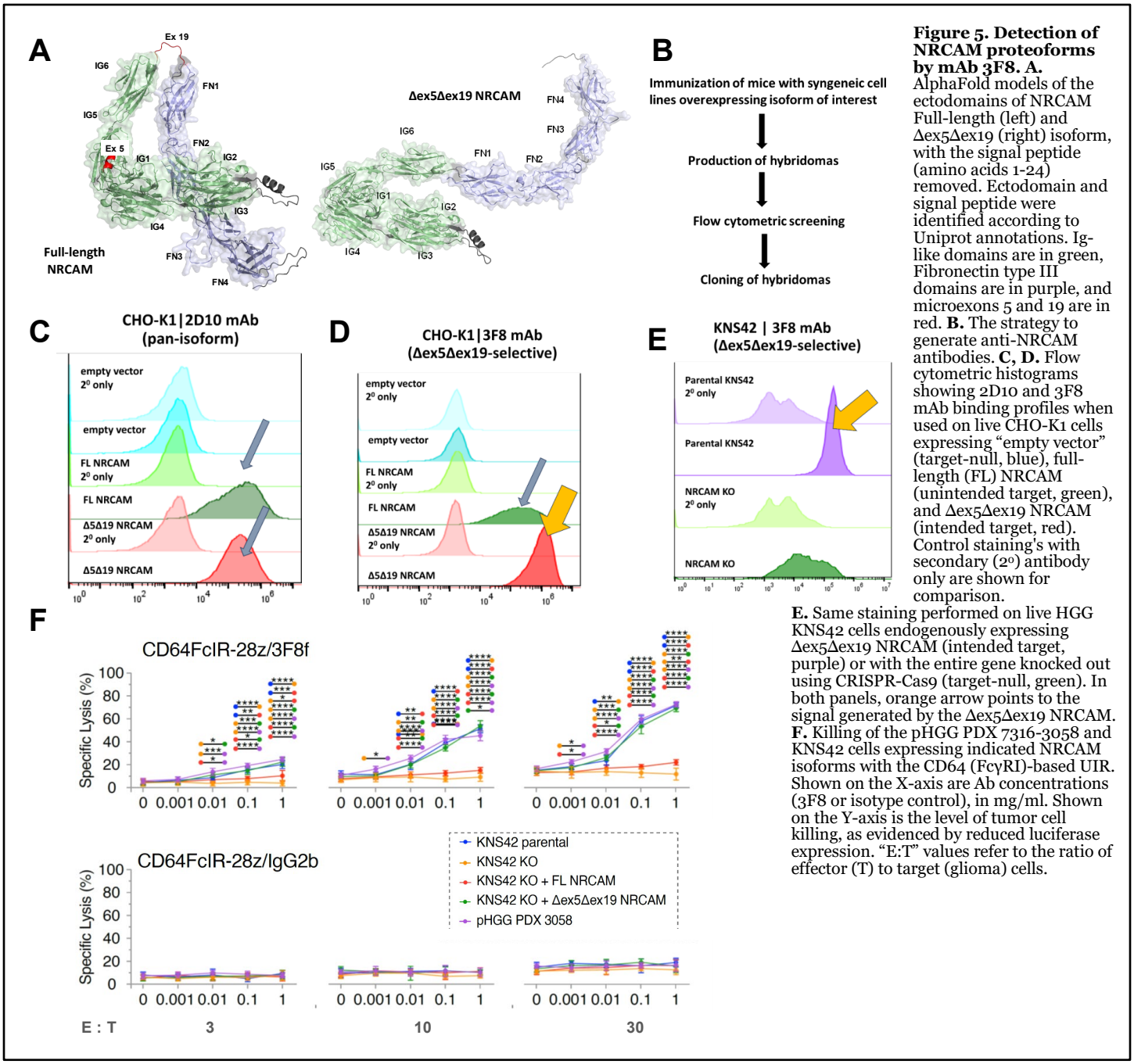

Figure 5. Detection of NRCAM proteoforms by mAb 3F8. A. AlphaFold models of the ectodomains of NRCAM Full-length (left) and Δex5Δex19 (right) isoform, with the signal peptide (amino acids 1-24) removed. Ectodomain and signal peptide were identified according to Uniprot annotations. Ig-like domains are in green, Fibronectin type III domains are in purple, and microexons 5 and 19 are in red. **B.** The strategy to generate anti-NRCAM antibodies. **C, D.** Flow cytometric histograms showing 2D10 and 3F8 mAb binding profiles when used on live CHO-K1 cells expressing "empty vector" (target-null, blue), full-length (FL) NRCAM (unintended target, green), and Δex5Δex19 NRCAM (intended target, red). Control staining's with secondary (2°) antibody only are shown for comparison. **E.** Same staining performed on live HGG KNS42 cells endogenously expressing Δex5Δex19 NRCAM (intended target, purple) or with the entire gene knocked out using CRISPR-Cas9 (target-null, green). In both panels, orange arrow points to the signal generated by the Δex5Δex19 NRCAM. **F.** Killing of the pHGG PDX 7316-3058 and KNS42 cells expressing indicated NRCAM isoforms with the CD64 (FcγRI)-based UIR. Shown on the X-axis are Ab concentrations (3F8 or isotype control), in mg/ml. Shown on the Y-axis is the level of tumor cell killing, as evidenced by reduced luciferase expression. "E:T" values refer to the ratio of effector (T) to target (glioma) cells.

To determine how efficient and selective 3F8-based immunotherapeutics might be, we applied a universal immune receptor (UIR) technology to redirect T cell specificity towards antibody-stained cells, as described by us previously (64). Specifically, we "painted" KNS42 cells with the 3F8 antibody and admixed them in vitro with human donor-derived T cells engineered to express a CD64 (FcγRI)-based UIR (65). We observed that this antibody-UIR combination could kill the majority of pHGG cells, but only when the cancer cells expressed the Δex5Δex19 NRCAM proteoform, ectopically or endogenously using KNS42 or PDX 7316-3058 (Figure 5F, top row). No killing was observed against cells expressing full-length NRCAM, when the FcγRI UIR was armed by an irrelevant isotype-control IgG2b antibody (Figure 5F, bottom row), or with un-transduced donor T cells (Supplemental Figure S2A). We further tested the 3F8-UIR combination against adult GBM cell lines U251 and TM31 (which exclusively express the Δex5Δex19 NRCAM isoform) and their *NRCAM* KO derivatives. We observed the same efficacy and selectivity of cell killing as seen with pHGG models (Supplemental Figure S2B). We thus concluded that mAb 3F8 is a promising immunotherapeutic for pediatric and adult tumors of glial origin.

Discussion

It is well-recognized that failures of adoptive cancer immunotherapies come in two flavors: effector cell-centric (e.g., T cell exhaustion) and target cell-centric (e.g., epitope loss or down-modulation) (66). The latter problem underscores the need for robust pipelines yielding alternative antigens for salvage immunotherapies. Traditionally, such pipelines focused either on discovery of lineage-specific markers (B cell-specific CD19, CD22, etc.) (67) or on identification of proteins overexpressed in tumors compared to their respective tissues of origin. While such "tumor-versus-normal" comparisons continue to yield viable therapeutic targets, for example DLK1 and GPC2 in high-risk neuroblastoma (68,69), GPC2 in CNS tumors (70), B7-H3 (CD276) and GD2 in diffuse intrinsic pontine glioma (DIPG) and DMG (15,20), GD2 in medulloblastoma (71), this approach might be entering the phase of diminishing returns, as existing microarray and RNA-seq datasets have been mined extensively already. Additionally, "tumor-versus-normal" comparisons often ignore expression of the target antigen in non-adjacent normal tissues, creating the potential for severe on-target, off-tumor toxicities (OTOT) (72). For CAR T cells, OTOT could be circumvented with locoregional delivery, but this approach may not be effective for antibody-drug conjugates and other soluble therapeutics.

All these limitations led the cancer immunotherapy field to look for alternative sources of tumor-specific epitopes, such as alternatively splicing (73,74). In a hallmark paper investigating splicing patterns across The Cancer Genome Atlas, it was estimated that in the average tumor there exist close to 1,000 unique "neojunctions" not typically found in normal samples profiled by the GTEx consortium (75). However, only a tiny fraction of them (~0.1%) generate peptides capable of being presented by major histocompatibility complex class I molecules.

In principle, this bottleneck could be bypassed by focusing on transmembrane proteins with large extracellular domains, which could be recognized by engineered T-cells independently of MHC class I presentation (76). However, it is not clear what fraction of alternatively spliced transcripts yields functional proteoforms able to reach the plasma membrane. In hematologic malignancies, for example, there are several examples where exon skipping results in either protein degradation [P2RX5 (77)] or its retention in the endoplasmic reticulum [CD19 (78,79), CD33 (80)]. Finally, even when alternative splicing-derived proteoforms are expressed on the cell surface, anti-peptide monoclonal antibodies directed against "neojunctions" might efficiently and specifically recognize the denatured protein [e.g., CD22 Δex5-6 (81)], but not necessarily its membrane-bound conformation. Thus, in most cases alternative splicing might be just as likely to drive resistance than to enable new therapies (82). However, not all alternative splicing events are created equal; and some of them, for example inclusion/skipping of microexons, have evolved to preserve protein structures while generating unique 3D conformations (28,40).

Here we report that in pediatric HGG, the pattern of microexon inclusion is markedly different from that observed in normal brain samples. In fact, microexon skipping was the only single-exon type of events with profound differences in ΔPSI values (>50%). By focusing further on SE events with high prevalence, we were able to identify members of the L1 family of cell adhesion molecules (62), including NRCAM, as being particularly strongly affected by alternative splicing. This is not completely surprising since NRCAM was recently shown to be the molecule with the greatest number of proteoforms in the developing mouse and human retinas (83). There is also some evidence that NRCAM and related CAMs might be implicated in tumor progression [reviewed in (84)]. However, the importance of individual proteoforms in either normal or development and cancerous growth has not been elucidated.

By focusing on concurrent skipping of *NRCAM* microexons 5 and 19, we were able to demonstrate that the corresponding proteoform is not only stable and present on the pHGG cell surface, but it promotes cell migration and invasion and is essential for progressive tumor growth in orthotopic mouse models. Remarkably, despite minimal amino acid changes, it is also antigenically distinct, as we were successful in generating a monoclonal antibody (3F8) with high selectively toward NRCAM Δex5Δex19. This selectivity manifested itself not only in flow cytometry experiments, but also in functional cell killing assays, where pHGG cells reconstituted with NRCAM Δex5Δex19 – but not the full-length isoform – were effectively killed by human T cells engineered to express an FcR-based universal immune receptor and redirected by an NRCAM Δex5Δex19-specific mAb. These findings provide the rationale for future development and preclinical testing of other 3F8-based immunotherapeutics, including CARs.

If 3F8-based immunotherapeutics prove to be as potent as current ones (e.g., B7-H3 CARs), targeting NRCAM Δex5Δex19 could be advantageous from the OTOT standpoint. Indeed, we observed that this mRNA isoform is expressed at lower levels in several normal tissues, including the adrenal gland. Even in normal brain samples,

which have sizable fractions of cells of glial origin , we failed to detect significant levels of *NRCAM* Δex5Δex19 expression, as judged by JPM counts (Figure 2B). In fact, the recently developed Cancer-Specific Exon Miner identified NRCAM as one of the six alternatively spliced proteoforms highly and specifically expressed in multiple solid and brain pediatric tumors at high prevalence (85). Our data indicate that the potential of NRCAM Δex5Δex19 as a therapeutic target is not limited to pediatric tumors and could include adult low-grade gliomas and GBMs, pheochromocytomas and paragangliomas, and also cancers of non-neural origins, such lung adenocarcinomas.

The rather broad spectrum of *NRCAM* Δex5Δex19 expression raises interesting questions about its contribution to neoplastic growth. It could be argued that skipping of microexons 5 and 19 in pHGGs simply reflects their glial, not neuronal origin; and that normal glia (and by extension, its malignant counterparts) simply don't express the RNA-binding protein machinery to include microexons. While there is some recent experimental and computational support for this "skipping by neglect" scenario (86), several lines of evidence indicate that it may not be universally applicable. First and foremost, the identity of cell(s) of origin for human HGG is often inferred from mouse lineage tracing experiments and therefore is not firmly established (87). Examination of molecular signatures frequently points to the role of oligodendrocytic progenitor cells (OPC), at least in certain anatomic locations, such as pons. In contrast, diffuse hemispheric gliomas (of which KNS42 is representative) are now thought to arise from interneuronal precursors (88). Second, even if most pHGG do arise from OPCs, glia-specific microexons also have been identified (89). Third, intermediate levels of *NRCAM* exon 19 (but not exon 5) inclusion in pheochromocytomas and paragangliomas revealed by MAJIQlopedia argue that these cassettes are dynamically and independently regulated to shape the neoplastic phenotypes of individual tumor types. For example, skipping of *NRCAM* microexons could regulate its interactions with other members of the L1-IgCAMs (62,90,91) and the metastasis-promoting proteins of the ERM family [ezrin/radixin/moesin; (92)]. Elucidation of these interactions could reveal additional opportunities for the targeting of alternative splicing in pediatric gliomas.

Methods

RNA seq analyses. All high-grade glioma pediatric brain tumor raw data were harvested from the database of Genotypes and Phenotypes (dbGAP) (accession number phs002517.v2.p2), which includes tumors from the Children's Brain Tumor Network (https://cbtn.org) and the Pediatric Neuro-Oncology Consortium (https://pnoc.us/). rMATS Turbo (v4.1.0) with GENCODE v39 GFF annotations was used to detect alternative splicing events. Paired comparisons were performed between each tumor sample and seven distinct control sets, including brain homogenate (Clontech, #636643), brain stem (Agilent, #540053, adult), fetal brain (Clontech, #636526), cerebellum (Asterand, #63559-1156128F), and occipital cortex (Asterand, #38061-113046A4). Additionally, publicly available datasets were incorporated, including fetal brain (SRR4787052) and pediatric normal cortex (SRR7268790, SRR7268791, SRR7268792). Aberrant splicing events were filtered to retain those with ≥10 junction read counts. The filtered results served as the basis for all downstream analyses.

For target discovery, we extracted all skipped exon (SE) splice events with a ΔPSI ≥ |0.30| or a ΔPSI ≥ 0.10 when the control PSI was <.10. Additionally, they had to meet significance thresholds (FDR and p-value of < 0.05) in all seven comparisons per tumor sample. We then generated BED files representing exons of interest and intersected them with UniProt protein domain topologies using Bedtools (v2.30.0), which allowed identification of exons corresponding to extracellular domains. Box plots were used to visualize splicing events altered in at least 40% of tumor samples, stratified by exon length into the following categories: 0–30 nt, 31–50 nt, 51–100 nt, and >100 nt. The plots were color-coded to denote splicing preference (i.e., inclusion or skipping). Scatter plots were generated using the ggscatter function to highlight microexons (<50 nucleotides). All downstream analyses were conducted using R v4.4.0, with plots generated using ggplot2 v3.5.1.

For the analysis of isoform expression levels, FASTQ files corresponding to GTEx samples and brain cell subpopulations were downloaded, respectively, from dbGaP (accession number phs000424.v10.p2.c1) and GEO (Project GSE73721) using sratoolkit. Reads were aligned using STAR (46) 2-pass mapping to hg38 genome and GENCODE v39 version . Junction per million (JPM) was calculated by collating "uniquely mapped reads" column from the "SJ.out.tab" files from the STAR aligner output. Uniquely mapped reads were divided by the total number of reads per sample to normalize these splicing junctions for each sample, as described by us recently (93).

Cell culture. The pediatric high-grade glioma cell line KNS42 (RRID:CVCL_0378) and other established pHGG cell lines were cultured in DMEM-F12 (GIBCO, #11320033) supplemented with 10% FBS (GIBCO, #26140079), 2 mmol/L L-glutamine (GIBCO, #25030081), and penicillin/streptomycin (GIBCO, #15140122) at 37°C and 5% CO2. After thawing, cells were authenticated by short tandem repeat analysis, tested for Mycoplasma using the EZ-PCR Mycoplasma Detection Kit (Biological Industries, #20-700-20), and used for up to 12 passages. Patient derived cells were cultured in DMEM-F12 supplemented with B27 supplement (ThermoFischer, #12587-010), N2 supplement (ThermoFischer, #175020-48), EGF recombinant protein (ThermoFischer, #PHG0311L), FGF recombinant protein (Peprotech, #100-18B), Heparin (Sigma, #H3149), 2 mmol/L L-glutamine, and penicillin/streptomycin at 37°C and 5% CO2.

RNA extraction and reverse transcription. Total RNAs were isolated using Maxwell RSC simplyRNA Cells kit with the Maxwell RSC48 Instrument (Promega, #AS1390) and reverse-transcribed using SuperScript IV (Invitrogen, #18090010). Primer sequences used for cDNA amplification are available upon request.

Oxford Nanopore Technologies (ONT) long-read direct cDNA sequencing. Total RNAs were isolated using Maxwell RSC simplyRNA Cell Kits (Promega, #AS1390). Approximately 500 ng of total RNA was used for direct cDNA (SQK-LSK114; Oxford Nanopore Technologies [ONT]) library preparation. Subsequently, each library was loaded into a PromethION Flow Cell R10.4.1 version (FLO-PRO114M; ONT) and sequenced using a PromethION 2 Solo (ONT) for 48 hours. Raw Fast5 files were converted to fastq with guppy (version 3.4.5), followed by alignment to the GENCODE version of hg38 (version 30) using minimap2 (version 2.18); the resulting bam file was visualized using the Integrative Genomics Viewer (version 2.11.0).

ONT targeted resequencing. For *NRCAM*, primers were designed to bind to exons present in all the isoforms to ensure full coverage of all alternative splicing events. 5ng of cDNA were amplified with the long LongAmp Taq 2X Master Mix (New England Biolabs) for 25 cycles. The resulting amplicons were subjected to amplicon-seq (SQKNBD112.24, ONT) library preparation. Subsequently, each library was loaded into a Spot-ON flow cell R9 Version (FLO-MIN112, ONT) and sequenced in a MinION Mk1C device (ONT) until it had at least 1000 reads per sample. Results were aligned using Minimap2 version 2.24-r1122 and visualized in IGV version 2.12.3. MisER, a splicing re-alignment tool (47) was run on ONT output files and reads were realigned using *NRCAM* RefSeq transcripts downloaded from UCSC genome browser. The flanking region parameter for Miser was 110. For isoform quantitation, ESPRESSO (49) was run with default settings on MisER-realigned BAM files.

Single-nuclei isoform RNA sequencing. Nuclei from pHGG patient-derived organoids were isolated as described previously (54,55) and processed using the Chromium Next Gem Single Cell Multiome ATAC + Gene Expression kit from 10X Genomics (kit PN-1000285, chip PN-1000230, dual index kit PN-1000215). For short-read sequencing, the Chromium Single Cell Multiome Gene Expression Library was performed by following the manufacturer's instructions, starting from 8,000 single-nuclei. It was then loaded on an Illumina NovaSeq 6000 with PE 2 × 100 paired-end kit, using the following sequencing read lengths: 28 cycles Read1, 10 cycles i7 index, 10 cycles i7 index, and 90 cycles Read2. For long-read sequencing, cDNA obtained from the 10X Genomics Single Cell Multiome ATAC + Gene Expression kit was used for amplification and exome enrichment as described previously (55). The amplified/enriched cDNA was then sequenced on the Oxford Nanopore Technology platform starting from ~200 fmol cDNA and using the Ligation Sequencing Kit (SQK-LSK114), according to the manufacturer's protocol (Nanopore Protocol, Amplicons by Ligation, version ACDE_9163_v114_revO_29Jun2022). The ONT library was loaded onto a PromethION sequencer by using PromethION Flow Cell (FLO-PRO114M) and sequenced for 72 h. Base-calling was performed with Guppy by setting the base quality score **>7.**

Genome editing. Single-guide RNAs targeting *NRCAM* exons 8 and 11 and CAS9 protein were obtained from Integrated DNA Technologies. Cas9 ribonucleoprotein complexes were assembled following manufacturer's recommendations. These ribonucleoprotein complexes were transfected into KNS42 and 7316-3058 cells using Lipofectamine CRISPR MAX Kit (Invitrogen, CMAX00001) following manufacturer's instructions. The effect of gRNA was determined by immunoblotting for NRCAM.

Plasmid constructs and viral infections. For *NRCAM* constructs, the coding sequence of the full-length isoform (NM_001193582.2/ENST00000413765.6) and Δex5Δex19 *NRCAM* (NM_005010.5/ENST00000351718.8) was synthesized and cloned into the lentiviral backbone (pTwistLentiSFFV puro) by Twist Biosciences. For viral particle production, 293T cells (ATCC) grown to 90% confluence in a 10-cm Petri dish were transfected with 10 µg of the *NRCAM* constructs, 2.5 µg of the pMD2.G (RRID:Addgene_12259) and 7.5 µg of the psPAX2, (RRID:Addgene_12260) using Lipofectamine 3000 (Invitrogen, #L3000001).

Supernatants were collected 48 hours after transfection, passed through 0.45-µm PVDF filters, and incubated for 48 hours with cells in media containing 10 µg/mL polybrene (MedChemExpress, #HY112735). After 48 hours, culture media were replaced, and cells were incubated with 1.5 µg/mL puromycin for selection. For FcIR-28z, transfection was performed with a plasmid mix containing the transfer plasmid encoding the Fc binding immune receptor (FcIR) fused to the intracellular TCR and co-stimulatory signaling domains (FcIR-28z), along with packaging plasmids pRSV.REV (RRID:Addgene_12253), pMD2.G, and pVSV-G (RRID:Addgene_138479) in a 15:18:18:7 mass ratio. Lentiviral supernatants were collected at 24- and 48-hours post-transfection, filtered through a 0.45 µm filter, and concentrated via ultracentrifugation at 25,000 rpm for 2.5 hours. The final viral preparation was stored at -80°C. Viral titers were determined by transducing HEK 293T cells (RRID:CVCL_0063), and results were expressed as Infection Units per milliliter (IU/mL).

Immunoblotting. Total cell lysates were prepared from cells using RIPA buffer with protease and phosphatase inhibitors (Pierce Halt Inhibitor Cocktail, Thermo Fisher Scientific, #78446). After protein transference to PVDF (Immobilin-p, Millipore, #IPVH00010), an anti-NRCAM antibody (Abcam, #191418) was used. Subsequently, recommended dilutions of horseradish peroxidase–conjugated secondary antibody (Cell signaling, #7076S) was applied. Enhanced chemiluminescence (Millipore, #WBKLS0500) was used to detect bands that were then captured by Chemiluminescence imager (GE Healthcare). Each sample was normalized to HRP conjugated β-actin (Cell Signaling Technology, #12262S) or GAPDH (Cell Signaling Technology, #3683S).

Isolation of Biotin-labeled Cell Surface Proteins. Cell surface biotinylation was performed using Pierce™ Cell Surface Biotinylation and Isolation Kit (Thermo fischer scientific, #A44390). Briefly, cells were grown to confluency in 10-well dishes, washed with PBS, and labeled with a non-cell-permeable sulfo-NHS biotin analog for 10 minutes at room temperature. After washing, ice cold TBS was added to the cells which were collected with a cell scraper, and clarified by centrifugation (500 × *g*, 5 min, 4 °C). To isolate biotin-labeled cell surface proteins, lysate (was added to Neutravidin agarose column and incubated for 30 minutes at room temperature. Eluted protein fractions were then analyzed by immunoblotting.

Cell proliferation, migration, and invasion assays. To assess proliferation, cells were seeded in white 96 well flat bottom plates at a density of 8000 cells per well. Cell viability was measured using the CellTitre-Glo (CTG) luminescent cell viability assay (Promega, #G7570). Luminescence was measured using Biotek Synergy 2 plate reader at 24, 48 and 72hrs. Corning BioCoat Cell Culture Inserts and Matrigel inserts (Corning, USA) were used for migration and invasion assays, respectively, as described in (58). Briefly, the inserts were rehydrated with plain DME-F12 for 2 h before use. 5–7×104 cells (treated with 10ug/ml of Mitomycin C) were trypsinized and resuspended in serum-free medium and then seeded onto 24-well transwell chambers with 8-µm pore membrane in 500 µL serum-free medium. The lower chamber contained medium supplemented with 10% FBS. After incubation for 22 h, the non-migrated/invaded cells on the upper side of membrane were removed with a cotton swab and the migrated/invaded cells stained with crystal violet and microphotographed.

Orthotopic mouse model. The orthotopic pHGG models have been described by us previously (59). Briefly, eight to 10-week-old Nu/J mice (8 animals per treatment group) were anesthetized with 2.5% isoflurane, placed into the stereotactic frame, then injected with $1x10^6$ glioma cells. Stereotactic coordinates used to target the cortex for tumor were as follows: -0.4 mm posterior to bregma, 3mm lateral to bregma, and 1 mm depth from pia. All animals were subjected to regular optical imaging beginning at 3 weeks post-injection.

AlphaFold analysis of NRCAM isoform structures. AlphaFold 3 (60) models were generated for the Uniprot-annotated ectodomains of the full-length and Δex5Δex19 NRCAM isoforms, specifically C9JYY6 and Q14CA1. The signal peptide at the N-terminus of the sequence (amino acids 1-24, identified in Uniprot) was removed before generating the models because these amino acids are cleaved in the ER during protein processing. Additionally, these isoforms lack the fifth fibronectin type-III domain, owning the exonic structures of the respective mRNAs (ENST00000413765.6 and ENST00000351718.8).

Generation of monoclonal antibody against NRCAM Δex5Δex19. All monoclonal antibodies were generated at the Fred Hutchinson Antibody Technology Core. Briefly, male and female 20-week-old mice were immunized with syngeneic NIH3T3 cells overexpressing Δex5Δex19 NRCAM. Following a 12+ week boosting protocol, splenocytes were isolated from high-titer-yielding mice and electrofused with FOX-NY myeloma cells. Hybridomas secreting isoform specific antibody were identified and isolated. Antibodies from the picked clones were validated for proteoform binding by flow cytometry using cell-based flow cytometry. Clone 3F8 was subcloned followed by validation for proteoform binding by cell-based flow cytometry using cells expressing

empty vector, full length and Δex5Δex19 NRCAM. Affinity purified IgG2b kappas from the hybridoma was further characterized by Western blot analysis and flow cytometry staining.

Generation of Primary T Cells with FcIR-28z. The activation, transduction, and expansion of primary T cells were carried out as previously described (94). All primary T cell studies were conducted under approval from the University of Pennsylvania Institutional Review Board (IRB). Identified donors provided informed consent, signing forms approved by the IRB. Briefly, primary human CD4+ and CD8+ T cells, obtained from healthy donors and purchased from the Human Immunology Core (University of Pennsylvania), were combined in a 1:1 ratio in complete medium (CM) supplemented with 100 IU/mL IL-2 (Prometheus Therapeutics and Diagnostics). On Day 0, the T cells were stimulated with anti-CD3/CD28 Dynabeads (Invitrogen) at a 1:1 bead-to-cell ratio. After 24 hours (Day 1), T cells were transduced with FcIR-28z lentivirus at a multiplicity of infection (MOI) of 5. The culture volume was doubled daily by the addition of fresh CM until Day 6, at which point the Dynabeads were removed via magnetic separation. Cells were maintained at a concentration of 0.75×10^6 cells/mL in IL-2 supplemented CM until Day 10, when IL-2 was withdrawn from the medium to complete the expansion process. The efficiency of T cell transduction was assessed on Day 10 by flow cytometry, analyzing for the surface expression of FcIR.

Cytotoxicity Assays. KNS42 and patient-derived target cell lines were transduced with a pGFP-luc-blasticidin plasmid and subsequently sorted for GFP-positive populations using fluorescence-activated cell sorting (FACS). Target cells were resuspended in serum-free complete medium (CM) at a concentration of 20^5 viable cells/mL, and 100 µL was plated per well in a white, opaque-walled, flat-bottom 96-well plate. Cells were cultured overnight at 37°C in 5% CO_2 to reach a confluency of approximately 70-80%. FcIR-28z effector cells were "painted" with the antibody 3F8f and its IgG2b isotype control at concentrations of 0, 0.001, 0.01, 0.1, and 1 µg/mL. The painting was performed at 37°C in 5% CO_2 for 45 minutes in PBS. Following antibody incubation, effector cells were washed three times in PBS and resuspended in serum-free CM.

To calculate the effector-to-target (E:T) ratio, three random target cell samples from each cell line were trypsinized and counted for live cells. Based on the counts, effector cells were added to the target cells at 3:1, 10:1, and 30:1 E:T ratios. The appropriate number of effector cells was resuspended in 100 µL of serum-free CM and added to the corresponding target cell groups. All conditions were tested in triplicate for each target cell line. Plates were centrifuged at 200g for 3 minutes and then incubated in a humidified incubator at 37°C with 5% CO_2 for 24 hours. Following incubation, 100 µL of medium was carefully removed from each well for further analysis.

For luminescence-based viability assessment, D-luciferin was resuspended in PBS at 900 µg/mL, and 20 µL was added to each well to achieve a final concentration of 150 µg/mL. The plates were placed on an orbital shaker (GeneMate) at 500 rpm for 3 minutes in the dark, then incubated for an additional 3 minutes at 37°C and 5% CO_2. Luminescence readings were obtained using a microplate reader (BioTek Synergy H4), and cytotoxicity was calculated using the following formula: (1 - luminescence (effector + target cells)/luminescence(target cells)) x 100.

Acknowledgements

This research has been supported by NIH grants U01 CA232563 and R03 CA293992 (to ATT), R03 DE033366 (to JLR), and UG3 CA290451 and RO1 EB026892 (to DJP Jr). Additional support was provided by a Cure Search for Children's Cancer Foundation Acceleration Initiative Award (to ATT), Cancer Research Society Next Generation of Scientists Award (to MQV), the Children's Brain Tumor Network, and the Chad Tough Foundation. JL further acknowledges support by the National Science Foundation Graduate Research Fellowship Program (NSF-GRFP, grant DGE-2236662).

References

1. Aggarwal P, Luo W, Pehlivan KC, Hoang H, Rajappa P, Cripe TP, . . . Cairo MS. Pediatric versus adult high grade glioma: Immunotherapeutic and genomic considerations. Front Immunol 2022;13:1038096.

2. Fine HA. Glioblastoma: Not Just Another Cancer. Cancer Discov 2024;14(4):648-52.

3. O'Rourke DM, Nasrallah MP, Desai A, Melenhorst JJ, Mansfield K, Morrissette JJD, . . . Maus MV. A single dose of peripherally infused EGFRvIII-directed CAR T cells mediates antigen loss and induces adaptive resistance in patients with recurrent glioblastoma. Sci Transl Med 2017;9(399).

4. Choi BD, Gerstner ER, Frigault MJ, Leick MB, Mount CW, Balaj L, . . . Maus MV. Intraventricular CARv3-TEAM-E T Cells in Recurrent Glioblastoma. N Engl J Med 2024;390(14):1290-8.

5. Ahmed N, Brawley V, Hegde M, Bielamowicz K, Kalra M, Landi D, . . . Gottschalk S. HER2-Specific Chimeric Antigen Receptor-Modified Virus-Specific T Cells for Progressive Glioblastoma: A Phase 1 Dose-Escalation Trial. JAMA Oncol 2017;3(8):1094-101.

6. Brown CE, Alizadeh D, Starr R, Weng L, Wagner JR, Naranjo A, . . . Badie B. Regression of Glioblastoma after Chimeric Antigen Receptor T-Cell Therapy. N Engl J Med 2016;375(26):2561-9.

7. Chow KK, Naik S, Kakarla S, Brawley VS, Shaffer DR, Yi Z, . . . Gottschalk S. T cells redirected to EphA2 for the immunotherapy of glioblastoma. Mol Ther 2013;21(3):629-37.

8. Petersen CT, Krenciute G. Next Generation CAR T Cells for the Immunotherapy of High-Grade Glioma. Front Oncol 2019;9:69.

9. Migliorini D, Dietrich PY, Stupp R, Linette GP, Posey AD, Jr., June CH. CAR T-Cell Therapies in Glioblastoma: A First Look. Clin Cancer Res 2018;24(3):535-40.

10. Larson RC, Maus MV. Recent advances and discoveries in the mechanisms and functions of CAR T cells. Nat Rev Cancer 2021;21(3):145-61.

11. Maggs L, Cattaneo G, Dal AE, Moghaddam AS, Ferrone S. CAR T Cell-Based Immunotherapy for the Treatment of Glioblastoma. Front Neurosci 2021;15:662064.

12. Patterson JD, Henson JC, Breese RO, Bielamowicz KJ, Rodriguez A. CAR T Cell Therapy for Pediatric Brain Tumors. Front Oncol 2020;10:1582.

13. Lin YJ, Mashouf LA, Lim M. CAR T Cell Therapy in Primary Brain Tumors: Current Investigations and the Future. Front Immunol 2022;13:817296.

14. Mount CW, Majzner RG, Sundaresh S, Arnold EP, Kadapakkam M, Haile S, . . . Mackall CL. Potent antitumor efficacy of anti-GD2 CAR T cells in H3-K27M(+) diffuse midline gliomas. Nat Med 2018;24(5):572-9.

15. Majzner RG, Ramakrishna S, Yeom KW, Patel S, Chinnasamy H, Schultz LM, . . . Monje M. GD2-CAR T cell therapy for H3K27M-mutated diffuse midline gliomas. Nature 2022;603(7903):934-41.

16. Majzner RG, Theruvath JL, Nellan A, Heitzeneder S, Cui Y, Mount CW, . . . Mackall CL. CAR T Cells Targeting B7-H3, a Pan-Cancer Antigen, Demonstrate Potent Preclinical Activity Against Pediatric Solid Tumors and Brain Tumors. Clin Cancer Res 2019;25(8):2560-74.

17. Straathof K, Flutter B, Wallace R, Jain N, Loka T, Depani S, . . . Anderson J. Antitumor activity without on-target off-tumor toxicity of GD2-chimeric antigen receptor T cells in patients with neuroblastoma. Sci Transl Med 2020;12(571).

18. Ladenstein R, Potschger U, Valteau-Couanet D, Luksch R, Castel V, Yaniv I, . . . Lode HN. Interleukin 2 with anti-GD2 antibody ch14.18/CHO (dinutuximab beta) in patients with high-risk neuroblastoma (HR-NBL1/SIOPEN): a multicentre, randomised, phase 3 trial. Lancet Oncol 2018;19(12):1617-29.

19. Du H, Hirabayashi K, Ahn S, Kren NP, Montgomery SA, Wang X, . . . Dotti G. Antitumor Responses in the Absence of Toxicity in Solid Tumors by Targeting B7-H3 via Chimeric Antigen Receptor T Cells. Cancer Cell 2019;35(2):221-37 e8.

20. Vitanza NA, Wilson AL, Huang W, Seidel K, Brown C, Gustafson JA, . . . Park JR. Intraventricular B7-H3 CAR T Cells for Diffuse Intrinsic Pontine Glioma: Preliminary First-in-Human Bioactivity and Safety. Cancer Discov 2023;13(1):114-31.

21. Labanieh L, Mackall CL. CAR immune cells: design principles, resistance and the next generation. Nature 2023;614(7949):635-48.

22. Wagner J, Wickman E, DeRenzo C, Gottschalk S. CAR T Cell Therapy for Solid Tumors: Bright Future or Dark Reality? Mol Ther 2020;28(11):2320-39.

23. Tousley AM, Rotiroti MC, Labanieh L, Rysavy LW, Kim WJ, Lareau C, . . . Majzner RG. Co-opting signalling molecules enables logic-gated control of CAR T cells. Nature 2023;615(7952):507-16.

24. Naqvi AS, Corbett RJ, Seghal P, Conkrite KL, Rathi KS, Ennis BM, . . . Rokita JL. Characterization of aberrant splicing in pediatric central nervous system tumors reveals CLK1 as a candidate oncogenic dependency. bioRxiv 2024.

25. Shapiro JA, Gaonkar KS, Spielman SJ, Savonen CL, Bethell CJ, Jin R, . . . Pacific Pediatric Neuro-Oncology C. OpenPBTA: The Open Pediatric Brain Tumor Atlas. Cell Genom 2023;3(7):100340.

26. Shen S, Park JW, Lu ZX, Lin L, Henry MD, Wu YN, . . . Xing Y. rMATS: robust and flexible detection of differential alternative splicing from replicate RNA-Seq data. Proc Natl Acad Sci U S A 2014;111(51):E5593-601.

27. Volfovsky N, Haas BJ, Salzberg SL. Computational discovery of internal micro-exons. Genome Res 2003;13(6A):1216-21.

28. Gonatopoulos-Pournatzis T, Blencowe BJ. Microexons: at the nexus of nervous system development, behaviour and autism spectrum disorder. Curr Opin Genet Dev 2020;65:22-33.

29. Irimia M, Weatheritt RJ, Ellis JD, Parikshak NN, Gonatopoulos-Pournatzis T, Babor M, . . . Blencowe BJ. A highly conserved program of neuronal microexons is misregulated in autistic brains. Cell 2014;159(7):1511-23.

30. Jbara A, Lin KT, Stossel C, Siegfried Z, Shqerat H, Amar-Schwartz A, . . . Karni R. RBFOX2 modulates a metastatic signature of alternative splicing in pancreatic cancer. Nature 2023;617(7959):147-53.

31. Li J, Choi PS, Chaffer CL, Labella K, Hwang JH, Giacomelli AO, . . . Hahn WC. An alternative splicing switch in FLNB promotes the mesenchymal cell state in human breast cancer. eLife 2018;7.

32. Head SA, Hernandez-Alias X, Yang JS, Ciampi L, Beltran-Sastre V, Torres-Mendez A, . . . Serrano L. Silencing of SRRM4 suppresses microexon inclusion and promotes tumor growth across cancers. PLoS Biol 2021;19(2):e3001138.

33. Conn VM, Gabryelska M, Marri S, Stringer BW, Ormsby RJ, Penn T, . . . Conn SJ. SRRM4 Expands the Repertoire of Circular RNAs by Regulating Microexon Inclusion. Cells 2020;9(11).

34. Quesnel-Vallieres M, Irimia M, Cordes SP, Blencowe BJ. Essential roles for the splicing regulator nSR100/SRRM4 during nervous system development. Genes Dev 2015;29(7):746-59.

35. Mochizuki Y, Funayama R, Shirota M, Kikukawa Y, Ohira M, Karasawa H, . . . Nakayama K. Alternative microexon splicing by RBFOX2 and PTBP1 is associated with metastasis in colorectal cancer. Int J Cancer 2021;149(10):1787-800.

36. Li YI, Sanchez-Pulido L, Haerty W, Ponting CP. RBFOX and PTBP1 proteins regulate the alternative splicing of micro-exons in human brain transcripts. Genome Res 2015;25(1):1-13.

37. Raj B, Irimia M, Braunschweig U, Sterne-Weiler T, O'Hanlon D, Lin ZY, . . . Blencowe BJ. A global regulatory mechanism for activating an exon network required for neurogenesis. Mol Cell 2014;56(1):90-103.

38. Morales J, Pujar S, Loveland JE, Astashyn A, Bennett R, Berry A, . . . Murphy TD. A joint NCBI and EMBL-EBI transcript set for clinical genomics and research. Nature 2022;604(7905):310-5.

39. Aguet F, Anand S, Ardlie KG, Gabriel S, Getz GA, Graubert A, . . . Volpi S. The GTEx Consortium atlas of genetic regulatory effects across human tissues. Science 2020;369(6509):1318-30.

40. Ustianenko D, Weyn-Vanhentenryck SM, Zhang C. Microexons: discovery, regulation, and function. Wiley Interdiscip Rev RNA 2017;8(4).

41. Quesnel-Vallieres M, Jewell S, Lynch KW, Thomas-Tikhonenko A, Barash Y. MAJIQlopedia: an encyclopedia of RNA splicing variations in human tissues and cancer. Nucleic Acids Res 2024;52(D1):D213-D21.

42. Vaquero-Garcia J, Aicher JK, Jewell S, Gazzara MR, Radens CM, Jha A, . . . Barash Y. RNA splicing analysis using heterogeneous and large RNA-seq datasets. Nat Commun 2023;14(1):1230.

43. Vivian J, Rao AA, Nothaft FA, Ketchum C, Armstrong J, Novak A, . . . Paten B. Toil enables reproducible, open source, big biomedical data analyses. Nat Biotechnol 2017;35(4):314-6.

44. Goldman MJ, Craft B, Hastie M, Repecka K, McDade F, Kamath A, . . . Haussler D. Visualizing and interpreting cancer genomics data via the Xena platform. Nat Biotechnol 2020;38(6):675-8.

45. Zhang Y, Sloan SA, Clarke LE, Caneda C, Plaza CA, Blumenthal PD, . . . Barres BA. Purification and Characterization of Progenitor and Mature Human Astrocytes Reveals Transcriptional and Functional Differences with Mouse. Neuron 2016;89(1):37-53.

46. Dobin A, Davis CA, Schlesinger F, Drenkow J, Zaleski C, Jha S, . . . Gingeras TR. STAR: ultrafast universal RNA-seq aligner. Bioinformatics 2013;29(1):15-21.

47. Liu Z, Zhu C, Steinmetz LM, Wei W. Identification and quantification of small exon-containing isoforms in long-read RNA sequencing data. Nucleic Acids Res 2023;51(20):e104.

48. Robinson JT, Thorvaldsdottir H, Wenger AM, Zehir A, Mesirov JP. Variant Review with the Integrative Genomics Viewer. Cancer Res 2017;77(21):e31-e4.

49. Gao Y, Wang F, Wang R, Kutschera E, Xu Y, Xie S, . . . Xing Y. ESPRESSO: Robust discovery and quantification of transcript isoforms from error-prone long-read RNA-seq data. Sci Adv 2023;9(3):eabq5072.

50. Sharon D, Tilgner H, Grubert F, Snyder M. A single-molecule long-read survey of the human transcriptome. Nat Biotechnol 2013;31(11):1009-14.

51. Au KF, Sebastiano V, Afshar PT, Durruthy JD, Lee L, Williams BA, . . . Wong WH. Characterization of the human ESC transcriptome by hybrid sequencing. Proc Natl Acad Sci U S A 2013;110(50):E4821-30.

52. Byrne A, Beaudin AE, Olsen HE, Jain M, Cole C, Palmer T, . . . Vollmers C. Nanopore long-read RNAseq reveals widespread transcriptional variation among the surface receptors of individual B cells. Nat Commun 2017;8:16027.

53. Karlsson K, Linnarsson S. Single-cell mRNA isoform diversity in the mouse brain. BMC Genomics 2017;18(1):126.

54. Gupta I, Collier PG, Haase B, Mahfouz A, Joglekar A, Floyd T, . . . Tilgner HU. Single-cell isoform RNA sequencing characterizes isoforms in thousands of cerebellar cells. Nat Biotechnol 2018;36(12):1197–202.

55. Hardwick SA, Hu W, Joglekar A, Fan L, Collier PG, Foord C, . . . Tilgner HU. Single-nuclei isoform RNA sequencing unlocks barcoded exon connectivity in frozen brain tissue. Nat Biotechnol 2022;40(7):1082-92.

56. Hu W, Foord C, Hsu J, Fan L, Corley MJ, Bhatia TN, . . . Tilgner HU. ScISOr-ATAC reveals convergent and divergent splicing and chromatin specificities between matched cell types across cortical regions, evolution, and in Alzheimer's Disease. bioRxiv 2024:2024.02.24.581897.

57. Stein AN, Joglekar A, Poon CL, Tilgner HU. ScisorWiz: visualizing differential isoform expression in single-cell long-read data. Bioinformatics 2022;38(13):3474-6.

58. Sehgal P, Lanauze C, Wang X, Hayer KE, Torres-Diz M, Leu NA, . . . Thomas-Tikhonenko A. MYC Hyperactivates Wnt Signaling in APC/CTNNB1-Mutated Colorectal Cancer Cells through miR-92a-Dependent Repression of DKK3. Mol Cancer Res 2021;19(12):2003-14.

59. Brosius SN, Manley W, Harvey K, Gallanaugh J, Rohacek D, Anderson S, De Raedt T. Interneurons that BiTE: Harnessing the migratory capacity of cortical inhibitory interneuron precursors to treat high-grade glioma. bioRxiv 2024:2024.04.29.591530.

60. Abramson J, Adler J, Dunger J, Evans R, Green T, Pritzel A, . . . Jumper JM. Accurate structure prediction of biomolecular interactions with AlphaFold 3. Nature 2024;630(8016):493-500.

61. Su XD, Gastinel LN, Vaughn DE, Faye I, Poon P, Bjorkman PJ. Crystal structure of hemolin: a horseshoe shape with implications for homophilic adhesion. Science 1998;281(5379):991-5.

62. Hortsch M, Nagaraj K, Mualla R. The L1 family of cell adhesion molecules: a sickening number of mutations and protein functions. Adv Neurobiol 2014;8:195-229.

63. Pattwell SS, Arora S, Cimino PJ, Ozawa T, Szulzewsky F, Hoellerbauer P, . . . Holland EC. A kinase-deficient NTRK2 splice variant predominates in glioma and amplifies several oncogenic signaling pathways. Nat Commun 2020;11(1):2977.

64. Urbanska K, Lanitis E, Poussin M, Lynn RC, Gavin BP, Kelderman S, . . . Powell DJ, Jr. A universal strategy for adoptive immunotherapy of cancer through use of a novel T-cell antigen receptor. Cancer Res 2012;72(7):1844-52.

65. Minutolo NG, Hollander EE, Powell DJ, Jr. The Emergence of Universal Immune Receptor T Cell Therapy for Cancer. Front Oncol 2019;9:176.

66. Uslu U, Castelli S, June CH. CAR T cell combination therapies to treat cancer. Cancer Cell 2024;42(8):1319-25.

67. Ang Z, Thomas-Tikhonenko A. Lymphoma immunotherapy: the garden of forking paths. Blood 2024;143(8):655-7.

68. Bosse KR, Raman P, Zhu Z, Lane M, Martinez D, Heitzeneder S, . . . Maris JM. Identification of GPC2 as an Oncoprotein and Candidate Immunotherapeutic Target in High-Risk Neuroblastoma. Cancer Cell 2017;32(3):295-309.

69. Hamilton AK, Radaoui AB, Tsang M, Martinez D, Conkrite KL, Patel K, . . . Diskin SJ. A proteogenomic surfaceome study identifies DLK1 as an immunotherapeutic target in neuroblastoma. Cancer Cell 2024;42(11):1970-82 e7.

70. Foster JB, Griffin C, Rokita JL, Stern A, Brimley C, Rathi K, . . . Bosse KR. Development of GPC2-directed chimeric antigen receptors using mRNA for pediatric brain tumors. J Immunother Cancer 2022;10(9):e004450.

71. Ciccone R, Quintarelli C, Camera A, Pezzella M, Caruso S, Manni S, . . . Locatelli F. GD2-Targeting CAR T-cell Therapy for Patients with GD2+ Medulloblastoma. Clin Cancer Res 2024;30(11):2545-57.

72. Flugel CL, Majzner RG, Krenciute G, Dotti G, Riddell SR, Wagner DL, Abou-El-Enein M. Overcoming on-target, off-tumour toxicity of CAR T cell therapy for solid tumours. Nat Rev Clin Oncol 2023;20(1):49-62.

73. Anczukow O, Allain FH, Angarola BL, Black DL, Brooks AN, Cheng C, . . . Thomas-Tikhonenko A. Steering research on mRNA splicing in cancer towards clinical translation. Nat Rev Cancer 2024;24.

74. Nejo T, Wang L, Leung KK, Wang A, Lakshmanachetty S, Gallus M, . . . Okada H. Challenges in the discovery of tumor-specific alternative splicing-derived cell-surface antigens in glioma. Sci Rep 2024;14(1):6362.

75. Kahles A, Lehmann KV, Toussaint NC, Huser M, Stark SG, Sachsenberg T, . . . Ratsch G. Comprehensive Analysis of Alternative Splicing Across Tumors from 8,705 Patients. Cancer Cell 2018;34(2):211-24 e6.

76. Pan Y, Phillips JW, Zhang BD, Noguchi M, Kutschera E, McLaughlin J, . . . Xing Y. IRIS: Discovery of cancer immunotherapy targets arising from pre-mRNA alternative splicing. Proc Natl Acad Sci U S A 2023;120(21):e2221116120.

77. Ang Z, Annette C, Schimdt C, Hayer K, Hasanali ZS, Torres-Diz M, . . . Thomas-Tikhonenko A. P2RX5-Directed CAR-T Cells for Genotype-Guided Treatment of Lymphoid and Plasma Cell Malignancies in Patients of African Ancestry. Blood 2024;144(Supplement 1):1033-.

78. Bagashev A, Sotillo E, Tang CH, Black KL, Perazzelli J, Seeholzer SH, . . . Thomas-Tikhonenko A. CD19 Alterations Emerging after CD19-Directed Immunotherapy Cause Retention of the Misfolded Protein in the Endoplasmic Reticulum. Mol Cell Biol 2018;38(21):e00383-18.

79. Sotillo E, Barrett DM, Black KL, Bagashev A, Oldridge D, Wu G, . . . Thomas-Tikhonenko A. Convergence of Acquired Mutations and Alternative Splicing of CD19 Enables Resistance to CART-19 Immunotherapy. Cancer Discov 2015;5(12):1282-95.

80. Lamba JK, Chauhan L, Shin M, Loken MR, Pollard JA, Wang YC, . . . Meshinchi S. CD33 splicing polymorphism determines gemtuzumab ozogamicin response in de novo acute myeloid leukemia: report from randomized Phase III Children's Oncology Group trial AAML0531. J Clin Oncol 2017;35(23):2674-82.

81. Zheng S, Gillespie E, Naqvi AS, Hayer KE, Ang Z, Torres-Diz M, . . . Thomas-Tikhonenko A. Modulation of CD22 Protein Expression in Childhood Leukemia by Pervasive Splicing Aberrations: Implications for CD22-Directed Immunotherapies. Blood Cancer Discov 2022;3(2):103-15.

82. Zheng S, Asnani M, Thomas-Tikhonenko A. Escape From ALL-CARTaz: Leukemia Immunoediting in the Age of Chimeric Antigen Receptors. Cancer J 2019;25(3):217-22.

83. Ray TA, Cochran K, Kozlowski C, Wang J, Alexander G, Cady MA, . . . Kay JN. Comprehensive identification of mRNA isoforms reveals the diversity of neural cell-surface molecules with roles in retinal development and disease. Nat Commun 2020;11(1):3328.

84. Cavallaro U, Christofori G. Cell adhesion and signalling by cadherins and Ig-CAMs in cancer. Nat Rev Cancer 2004;4(2):118-32.

85. Shaw TI, Wagner J, Tian L, Wickman E, Poudel S, Wang J, . . . Gottschalk S. Discovery of immunotherapy targets for pediatric solid and brain tumors by exon-level expression. Nat Commun 2024;15(1):3732.

86. Seong M, Bak-Gordon P, Liu Z, Canoll PD, Manley JL. Splicing dysregulation in glioblastoma alters the function of cell migration-related genes. Glia 2025;73(2):251-70.

87. Alcantara Llaguno SR, Parada LF. Cell of origin of glioma: biological and clinical implications. Br J Cancer 2016;115(12):1445-50.

88. Liu I, Alencastro Veiga Cruzeiro G, Bjerke L, Rogers RF, Grabovska Y, Beck A, . . . Filbin MG. GABAergic neuronal lineage development determines clinically actionable targets in diffuse hemispheric glioma, H3G34-mutant. Cancer Cell 2024.

89. Reixachs-Sole M, Ruiz-Orera J, Alba MM, Eyras E. Ribosome profiling at isoform level reveals evolutionary conserved impacts of differential splicing on the proteome. Nat Commun 2020;11(1):1768.

90. Hortsch M. Structural and functional evolution of the L1 family: are four adhesion molecules better than one? Mol Cell Neurosci 2000;15(1):1-10.

91. Grumet M. Nr-CAM: a cell adhesion molecule with ligand and receptor functions. Cell Tissue Res 1997;290(2):423-8.

92. Duncan BW, Murphy KE, Maness PF. Molecular Mechanisms of L1 and NCAM Adhesion Molecules in Synaptic Pruning, Plasticity, and Stabilization. Front Cell Dev Biol 2021;9:625340.

93. Torres-Diz M, Reglero C, Falkenstein CD, Castro A, Hayer KE, Radens CM, . . . Thomas-Tikhonenko A. An Alternatively Spliced Gain-of-Function NT5C2 Isoform Contributes to Chemoresistance in Acute Lymphoblastic Leukemia. Cancer Res 2024;84(20):3327-36.

94. Smole A, Benton A, Poussin MA, Eiva MA, Mezzanotte C, Camisa B, . . . Powell DJ, Jr. Expression of inducible factors reprograms CAR-T cells for enhanced function and safety. Cancer Cell 2022;40(12):1470-87 e7.